Q. J. R. Meteorol. Soc. (2005), **131**, pp. 1655–1676 doi: 10.1256/qj.03.129

Sensitivity of one-dimensional radiative biases to vertical cloud-structure assumptions: Validation with aircraft data

By F. DI GIUSEPPE*

Environmental Systems Science Centre, University of Reading, UK
ARPA-Servizio IdroMeteorologico, Bologna, Italy

(Received 24 July 2003; revised 14 October 2004)

SUMMARY

Three representations of an observed stratocumulus system are generated by combining aircraft observations with a simple statistical model. The realizations differ in their representation of the vertical cloud structure while the horizontal variability is identical. In the control case (A) both the adiabatic liquid-water profile and the effect of wind-shear induced vertical decorrelation are represented. The second simulation (B) removes the wind-shear effect by assuming maximum overlap between adjacent layers. The third case (C) instead removes vertical variability by averaging the in-cloud liquid water for each column. For each of these scenes Monte Carlo simulated solar fluxes are compared against observed flux measurements. Cases A and B agree with observed (horizontal) flux variations within statistical uncertainty, while case C, which neglects vertical variability, is not able to reproduce the observed fluxes. The comparison between the radiative fields produced by these three representations of the stratocumulus system, calculated using a three-dimensional radiative-transfer solution, an independent pixel approximation (IPA) and a plane-parallel (PP) approach, shows substantial differences. Not accounting for the adiabatic liquid-water profile generates a systematic increase in the optical depth, τ when the effective radius is computed from mean liquid-water content and droplet-number concentration, that can be responsible for a 5% increase in the reflection for shallow boundary-layer cloud systems ($\tau \approx 1$). A much stronger effect in the radiative properties is produced by varying the cloud-overlap rule applied. While changing from maximum to random overlap does not introduce any variation in the optical depth of the cloud scene, it does introduce an increase in the reflection that is proportional to the relative change in total cloud fraction. The magnitude of these latter biases is comparable to that produced by unresolved horizontal variability. Moreover, it is shown that, when the vertical cloud structure is properly resolved, the effect of horizontal fluctuations is also reduced.

KEYWORDS: Cloud variability Three-dimensional radiation

1. INTRODUCTION

To quantify the radiative biases produced by unresolved spatial variability of clouds it is common practice to perform separate radiative-transfer calculations through a given cloud field, for which subgrid-scale inhomogeneities are progressively neglected (e.g. Cahalan *et al.* 1994a). Three methods are usually employed: a full three-dimensional (3D) calculation, an independent pixel approximation (IPA) approach and, lastly, a plane-parallel (PP) method, as is usually implemented in general-circulation models (GCMs) (Morcrette 1991). Specifically, the difference between the IPA and PP calculations is used to evaluate the influence of horizontal in-cloud inhomogeneity (the PP bias) while the 3D/IPA contrast assesses the effect of horizontal photon transport due to the geometrical organization of the cloud field (the IPA bias). From the analysis of the two different biases it is possible to quantify in which metric the mean radiative properties of the atmosphere are affected by the cloud unresolved geometrical arrangement and/or their optical internal inhomogeneities.

This technique has been extensively applied to quantify 3D radiative biases in different cloud regimes, such as stratocumulus (Cahalan *et al.* 1994a; Titov 1998; Di Giuseppe and Tompkins 2003b) shallow convection (Chambers *et al.* 1997) and deep convection (Fu *et al.* 2000; Barker *et al.* 1998, 1999; Di Giuseppe and Tompkins 2003a), leading sometimes to conflicting assessments of their significance for parametrization

* Corresponding address: Francesca Di Giuseppe, ARPA-SIM, Viale Silvani 6, 40128 Bologna, Italy.
e-mail: fdigiuseppe@smr.arpa.emr.it

in atmospheric models. The different assumptions underlying the cloud-field representation can be regarded as a possible explanation for those discrepancies. It is clear that the magnitude of 1D biases not only depends on the sensitivity of the chosen diagnostics to changes in cloud structures, but also on the realism of the cloud representation itself. To take an extreme case, one unrealistic representation of a cloud would be to assume it as homogeneous and infinitely extended, for which the 3D, IPA and PP calculations give identical results, implying null 1D biases.

Observations and numerical or idealized models all provide only a partial and inexact representation of cloud structures and can, therefore, potentially distort 1D bias estimations when used in 3D radiative studies. For overcast stratocumulus (Sc) regimes many authors used a bounded-cascade model, which produces a linear log–log power spectrum (Cahalan and Snider 1989; Cahalan and Joseph 1989; Albrecht *et al.* 1995; Pincus *et al.* 1999; Los and Duynkerke 2000, 2001). Using such a model, Cahalan *et al.* (1994b) and Barker and Davies (1992) claimed that the nonlinearity of the albedo with increasing liquid-water path (LWP) is responsible for a substantial PP biases of around 15%, while the IPA bias can be considered negligible. In their reconstruction, the important assumptions were made that cloud vertical variability could be neglected and that both upper and lower cloud boundaries were horizontal planes (the optical depth is thus only a function of the horizontal coordinates). Employing a new idealized model (SITCOM) Di Giuseppe and Tompkins (2003a) showed how these bias assessments could be affected by such approximations. While the IPA bias was confirmed to be limited, the PP bias was found to be substantially smaller if a representation of the vertical cloud structure is included and the stratocumulus adiabatic vertical liquid profile resolved.

The aim of this paper is to extend that investigation by examining in a more systematic way, and with the aid of observations, how the accuracy in the representation of Sc vertical variability can affect the radiative calculation and, ultimately, 1D bias estimations. Three proxies of the same cloud field are produced by employing SITCOM and the microphysical measurements collected by the Met Office C-130 Hercules aircraft over ocean areas near Cornwall (United Kingdom). The control case (case A) includes both the representation of the adiabatic liquid-water profile and the vertical decorrelation produced by horizontal wind shear, the second experiment (case B) only includes the adiabatic liquid-water content (LWC) and maximum overlap is assumed between adjacent layers. Finally, the third representation (case C) is obtained by vertically averaging the in-cloud liquid water in order to create a vertically homogeneous cloud. The latter is thus equivalent to the representation produced by a cascade model

Essentially, the three reconstructed cloud fields are generated by progressively removing available information on the cloud vertical structures while maintaining the same horizontal variability. Therefore, the differences in their radiation fields provide an insight as to how erroneous assumptions concerning the cloud-layer vertical overlap or unresolvable LWC profiles can affect the radiative calculations. These biases can then be related to those produced by the neglect of horizontal inhomogeneities by comparing the radiative fields obtained with 3D, IPA and PP calculations.

The ability of the reconstruction process to match the vertical and horizontal variability of the observed Sc system is verified through comparison between the variability of Monte Carlo fluxes calculated for the reconstructed cloud scenes and the observed fluxes.

After introducing the 3D radiative Monte Carlo code in section 2, the aircraft data and of the processing methodology are described in sections 3 and 4. The performance of the three cloud-field representations in reproducing the observed flux variability is

discussed in section 5. Section 6 examines the difference in the mean radiative fields and the implications of the reconstruction processes for 1D bias estimations. Finally, section 7 draws the conclusions of this study.

2. Radiative calculation

The radiative-transfer calculations have been performed using a modified version of the forward Monte Carlo algorithm (GRIMALDI). Details of the main code can be found in papers by Macke *et al.* (1997), Scheirer and Macke (2001) and Di Giuseppe and Tompkins (2003b); therefore, in the interest of brevity, only the basic radiative assumptions used and the achievable accuracy are reported here.

Water droplets are assumed spherical and the radiative interaction is described by Mie theory; a Gamma distribution is used as size-distribution function. Atmospheric absorption is included and a broadband spectral calculation has been added to GRIMALDI using the k-distribution model of Fu and Liou (1992). Five bands cover the solar part of the spectrum (0.2–3.5 μm). In this study the gaseous absorption is assumed to be horizontally homogeneous, implying that only one absorption coefficient is calculated for each vertical layer. Above the cloud domain, additional atmospheric levels are placed between 5 km (flight upper boundary) and 100 km, and profiles of absorbing gases and temperature are interpolated using mid-latitude standard profiles (McClatchey *et al.* 1972).

The accuracy of the model calculation is driven by the angular resolution (number of angles N in which the total phase function is sampled) and the number of statistical events simulated. This study adopts an angular resolution of $N = 181$. Using $O(10^6)$ photons is sufficient to guarantee a 0.5% accuracy in domain-averaged quantities, while 10^8 photons are used for a reliable estimation of three-dimensional flux fields.

3. Aircraft data

(*a*) *Data description*

The data used in this study were collected by the Met Office C-130 Hercules aircraft over sea areas near Cornwall on 22 February 2001 between 1200 UTC and 1500 UTC. Figure 1 shows the location and trajectory of the flight and the corresponding visible channel METEOSAT image recorded at 1330 UTC. The synoptic situation during the flight (A817) showed low-level stratocumulus clouds extending between 450 and 800 m. No high-level clouds were reported that could have affected the solar incoming radiation. Satellite retrieval measurements recorded an LWP of approximately 180 gm^{-2} for the cloud deck considered (Lin and Rossow 1994).

Standard flight parameters such as altitude and speed are obtained from the aircraft navigation equipment. The vapour mixing ratio is derived from the dew-point measurement; supersaturated values (q_s) exceeding 5% are considered inaccurate and are reset to this limit, since high supersaturated values are rarely found in warm clouds.

The cloud microphysics properties were recorded both using a fast Forward Scattering Spectrometer Probe (FSSP) and a Nevzorov Probe. The comparison between the FSSP and the Nevzorov Probe liquid-water values shows discrepancies smaller than 10%. The mean water-droplet concentration number recorded during the flight was 130 cm^{-3}, this value was almost constant throughout the vertical extend of the cloud. Effective radii ranging between 8 and 14 μm were observed. Integrated hemispheric upward and downward fluxes were collected using a Precision Spectral Pyranometer (PSP) for almost the whole solar spectrum (0.3–3.0 μm).

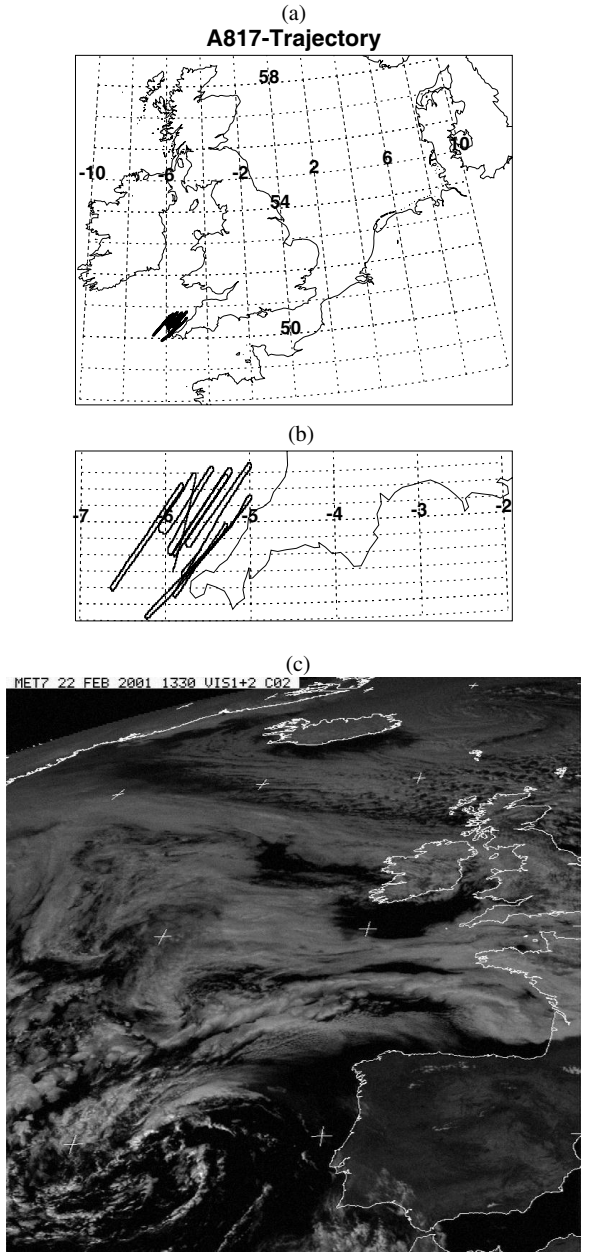

Figure 1. (a) The location and (b) the trajectory of flight A817 used in this study. The data were collected by the Met Office C-130 Hercules aircraft over sea areas near Cornwall (United Kingdom) on 22 February 2001 between 1200 UTC and 1500 UTC. (c) The corresponding visible channel METEOSAT image at 1330 UTC (source http://badc.nerc.ac.uk/).

The dataset was measured at 1 Hz, giving maximum horizontal resolution (i.e. neglecting sensor lag) of approximately 100 m, according to an aircraft velocity of 100 m s^{-1}.

(*b*) *Data processing*

The mean temperature and total-water profiles during the flight are calculated by horizontally averaging the whole set of quality controlled data. With the same procedure, the mean wind profiles in the vertical (w) and horizontal (u) directions are also deduced. The presence of wind shear implies that vertical decorrelation between adjacent cloud layers is expected to occur.

The variability of the total water anomaly field (q_t') is determined by examining several power spectra ($\mathcal{P}_W$) along horizontal legs at different altitudes inside the cloud. In agreement with satellite observations (e.g. Cahalan and Snider 1989) of LWP, this analysis shows that, with good approximation, the total-water field power spectra also have a power-law dependency with wavenumber (k) that can be expressed in the form $\mathcal{P}_W \propto k^{-\beta}$, where the constant β quantifies the energy cascade.

The smallest resolvable spatial scale of the q_t' field is twice the measurement resolution (200 m) (the 'Nyquist frequency') while the lowest frequency (largest spatial scale) present in the power spectrum relates to the length of the path across the cloud over which the power spectrum is calculated. Testing the power spectrum slope at different leg-lengths is important in order to check that both β and the low-frequency cut-off are independent of the sampling procedure.

The flight data are then divided into level-flight segments or 'legs' of a specified length, $\mathcal{L}$. The pressure altitude must not deviate by more than 5 hPa from the pressure registered at the leg beginning for the stretch of data analysed to be validated as a leg. Tests made using alternative tolerances of 2 hPa and 10 hPa show that the conclusions are not greatly affected by the choice of this parameter. If this criterion is broken before the required leg-length is achieved, the data in that segment are rejected. Additionally an identical dataset is used in each leg-length analysis. This is accomplished by first analysing the data using the longest leg-length of 40 km. All subsequent shorter leg-lengths of 3, 10 and 20 km use only the data contained in the 40 km legs. Although this involves the rejection of significant amount of data, (i.e. straight flight segments shorter than 40 km), this is found to be crucial for relating univocally eventual differences in the power spectrum slopes uniquely to the sampling methodology. With these rules a total of 13 legs of 40 km length were obtained along the whole flight trajectory, four of which were inside cloud.

Some previous studies have attempted to isolate mesoscale variability with scales exceeding leg-length by removing the linear trend (calculated using a least squares fit over each leg) (e.g. Nucciarone and Young 1991). The statistics in this paper were calculated twice, first using raw data (which were compared with statistics using detrended data) where the trends in total-water variability were calculated over the maximum leg-length of 40 km. The difference was of minor importance and did not impact the definition of the parameters used to characterized cloud variability.

Figure 2 gives an overview of the parameters measured during the flight. The flight consisted of a number of constant altitude legs, interspersed by longer descending or ascending runs through the cloud. The latter are all rejected by the data-processing algorithm, since the altitude changes by more than the specified limits before a 40 km leg is complete (between 250 and 300 km for example). The decrease of the incoming solar radiation during the flight, due to the increase of the solar zenith angle (SZA) as the flight proceeds in the afternoon, is noticeable. The upwelling fluxes recorded at altitudes

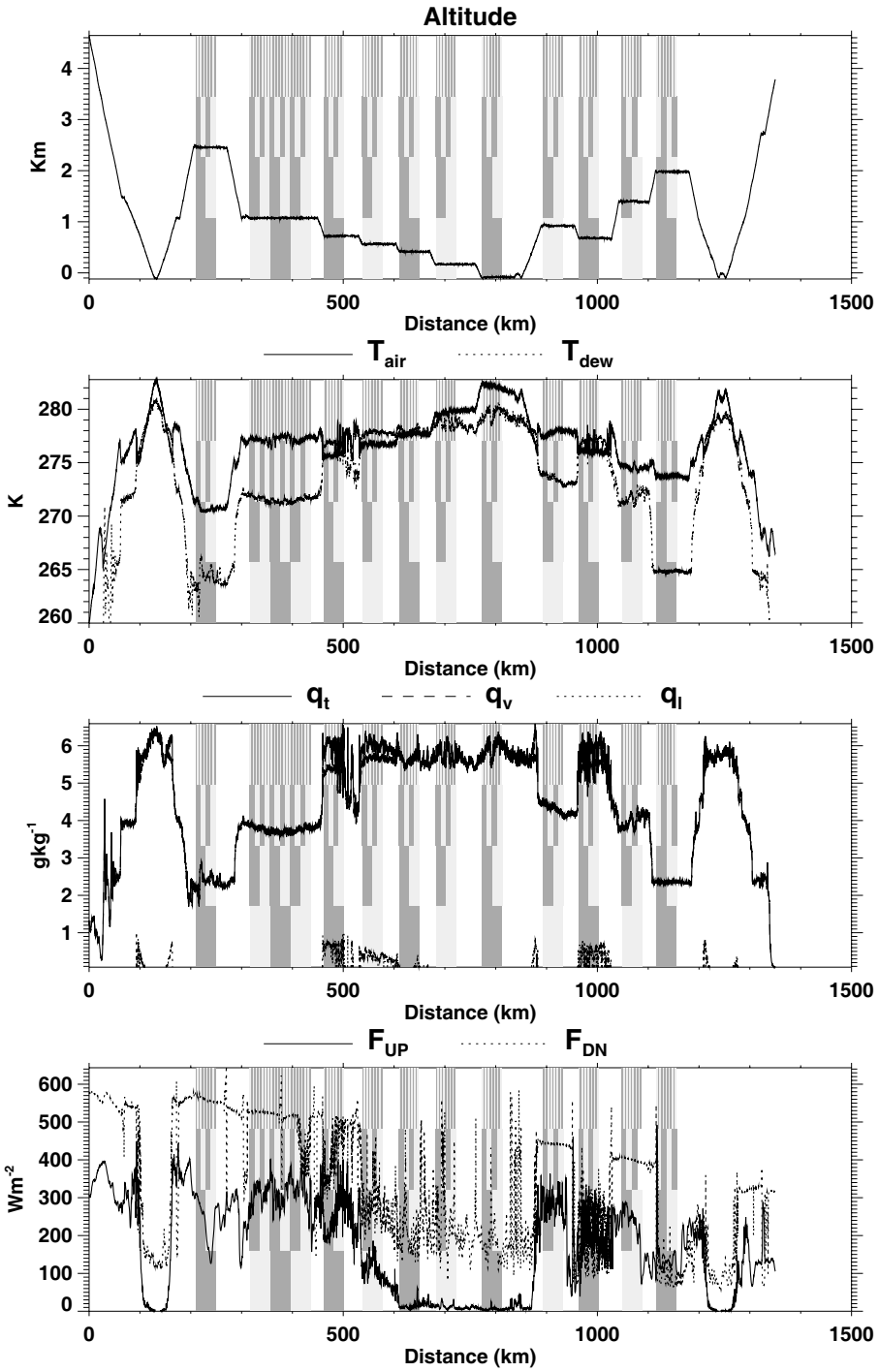

Figure 2. Overview of the altitude, the dry and dew-point temperatures (T_{air} and T_{dew}), the total-water, water-vapour and liquid-water mixing ratios (q_t, q_v and q_l), and the upward and downward short-wave fluxes (F_{up} and F_{down}) recorded during flight A817. The legs ($\mathcal{L} = 40$, 20, 10 and 3 km) within which the data have been divided are indicated with vertical bars.

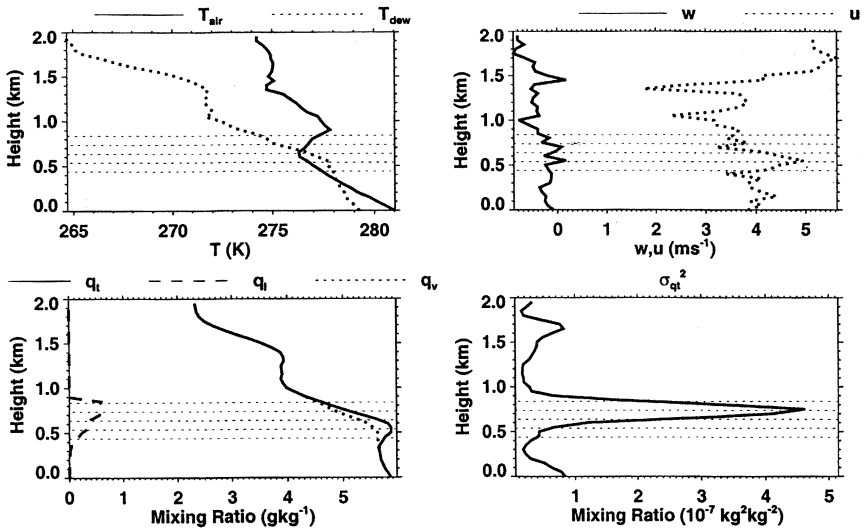

Figure 3. Vertical profiles of the mean thermodynamical quantities for flight A817: (a) the dry and dew-point temperatures ($T_{\rm air}$ and $T_{\rm dew}$), (b) the vertical and horizontal velocities (w and u), (c) the total-water, water-vapour and liquid-water mixing ratios ($q_{\rm t}$, $q_{\rm v}$ and $q_{\rm l}$), and (d) the total-water variance ($\sigma^2_{q_{\rm t}}$). The levels at which the reconstructed clouds are generated are indicated by horizontal dotted lines.

smaller than the cloud base are almost negligible due to the dark background provided by the ocean underneath.

The estimated surface albedo is around 3%. Vertical profiles of the mean thermodynamical quantities for the flight considered here are shown in Fig. 3. They reveal that the cloud base was around 500 m, from which the liquid water increases approximately monotonically (linear profile) to a peak value around 0.6 g kg^{-1} near cloud top at 800 m. There is some evidence of a weak temperature inversion capping the cloud layer. The figure also shows the vertical profile of the total-water variance obtained by interpolating the values derived from the 40 km legs. In the upper part of the same plot the wind profiles in the x and z directions are shown. The horizontal wind component is almost one order of magnitude larger than the mean vertical velocity. This is not atypical and the decorrelation height inside the cloud can be small (Hogan and Illingworth 2000).

In Fig. 4 the absolute value of the power-spectrum slope, β, is reported. The value of β is not strongly affected by the dimensions of the leg-lengths (Marshak *et al.* 1997a; Davis *et al.* 1997) while, interestingly, its value increases as the leg is located at higher altitude and the variance of the total water reaches its maximum.

4. Simulated cloud field

From the aircraft one-dimensional data, three possible reconstructions of the cloud field are generated using the Spectral Idealized Thermodynamically COnsistent Model (SITCOM). A 2-D field of total-water variability, $q'_{\rm t}(x, y)$, is generated possessing the same statistics as those of the observed cloud fields. By replicating this generation procedure at each model level, it is guaranteed that the vertical structure of the cloud is included in a thermodynamically coherent way. Details of the model can be found in Di Giuseppe and Tompkins (2003b).

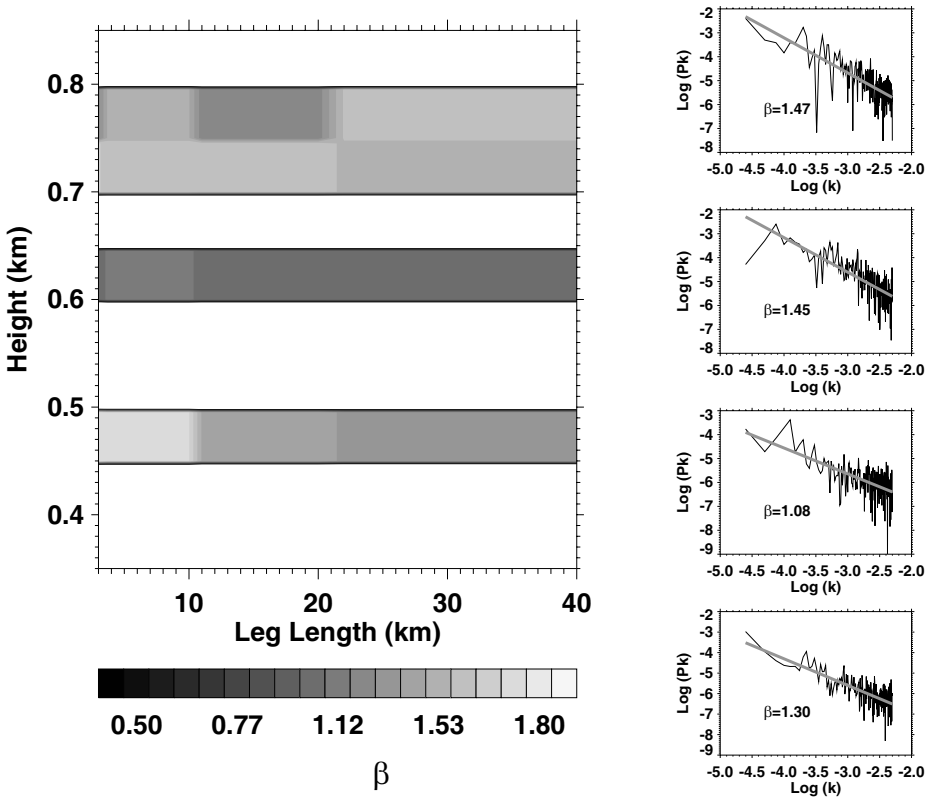

Figure 4. The left-hand panel indicates the absolute values of the power-spectrum slope, β, as function of the leg-height and length for the 3, 10, 20 and 40 km legs (shading levels as in the key). The in-cloud power spectra calculated for the four legs of 40 km length are shown in the right-hand panels, together with linear-regression lines.

At each vertical layer, a total-water anomaly field, $q_t'(\nu_x, \nu_y)$, is generated by defining a power-law function in the frequency space according to:

$$\mathcal{P}_W(r_\nu) \approx \sigma_{q_t}^2 r_\nu^{-\beta}\, e^{-(r_{\nu_0}/r_\nu)^n}, \tag{1}$$

with $r_\nu = (\nu_x^2 + \nu_y^2)^{\frac{1}{2}}$, where ν_x and ν_y are frequencies in the x and y directions, respectively. This functional choice reproduces the observation of a power-law dependency of the total-water variability anomaly field with the frequency scales along the aircraft legs. Nevertheless, a simple log–normal function has not been chosen because observations of peaked spectra of stratocumulus LWC fields have been documented (Wood and Taylor 2001). Equation (1) allows the incorporation of such a long-wavelength cut-off and, in this sense, is more general than a simple power-law function. In fact, the frequency r_{ν_0} in Eq. (1) defines a peak position in the frequency space. When r_{ν_0} has a value smaller than $1/L$, with L the domain horizontal dimension, a preferred scale for the total-water variability is created. The parameter n controls the long-wavelength cut-off. Since no preferred scale was observed during this flight, a value of $r_{\nu_0} = 1/L$ has been imposed. Similarly $n = 1$ is used. The value of β is set to the mean of the four 40 km legs of aircraft observations. Finally, a random white-noise function $\mathcal{R}$ is added to the above equation to break the symmetry of the real-space field (Di Giuseppe and

Tompkins 2003b). The total-water anomaly field, $q'_{\mathrm{t}}(\nu_x, \nu_y)$, in the frequency space is then transformed to the real space to give a two-dimensional field for $q_{\mathrm{t}}(x, y)$.

The power-spectrum integral over the whole frequency domain represents the total variance ($\sigma^2_{q_{\mathrm{t}}}$) associated with the $q_{\mathrm{t}}(x, y)$ field. Values for ($\sigma^2_{q_{\mathrm{t}}}$) are taken from the 13 legs of aircraft measurements, as shown in Fig. 3, and are used to rescale Eq. (1) at each vertical level in order to ensure the consistency between observed and simulated total-water variance profiles.

The mean atmospheric temperature and $\overline{q_{\mathrm{t}}}$ profiles are used to initialize the model. No horizontal temperature variability is included; consequently the saturation mixing ratio ($\overline{q_{\mathrm{s}}}$) is constant at each vertical layer. Price and Wood (2002) and Tompkins (2003) showed that, in most cases, this is an acceptable assumption since total-water variability is larger than that of q_{s}. The two-dimensional fields for total water and liquid cloud for a defined height z can be expressed in the form:

$$q_{\mathrm{t}}(x, y) = q'_{\mathrm{t}}(x, y) + \overline{q_{\mathrm{t}}} \tag{2}$$

$$q_{\mathrm{l}}(x, y) = q_{\mathrm{t}}(x, y) - \overline{q_{\mathrm{s}}}. \tag{3}$$

With this approach, the mean value of $q_{\mathrm{t}}(x, y)$ and its variance are imposed to be equal to the observed ones. Nevertheless, $\overline{q_{\mathrm{l}}}$ will not be, in general, coincident with the measured value (reported in Fig. 3) since the higher moments of the $q_{\mathrm{t}}(x, y)$ distribution, $G(q_{\mathrm{t}})$ (e.g. skewness and kurtosis) remain unknown and the spatial variability of q_{s} has been neglected. The disagreement between the derived and the measured cloud water increases with the skewness of the total water distribution (Wood and Field 2000).

To avoid this mismatch, $\overline{q_{\mathrm{s}}}$ is replaced by a corrected saturation mixing ratio, q^*_{s}, within each cloudy layer so that:

$$|\overline{q_{\mathrm{l}}}^{\mathrm{simulated}} - \overline{q_{\mathrm{l}}}^{\mathrm{measured}}| < \varepsilon_{q_{\mathrm{l}}}, \tag{4}$$

where $\varepsilon_{q_{\mathrm{l}}} = 0.1$ g kg^{-1} is a fixed tolerance value and

$$\overline{q_{\mathrm{l}}}^{\mathrm{simulated}} = \int_{q^*_{\mathrm{s}}}^{\infty} G(q_{\mathrm{t}})\, \mathrm{d}q_{\mathrm{t}}.$$

With this approximation, the dry-bulb temperature, T^*, (defined by $q_{\mathrm{s}}(T^*)$) differs from the aircraft measured value by at most 0.5 K, which is the nominal accuracy of the Rosemount temperature probe (Feind *et al.* 2000; Wood and Field 2000).

A 'reconstructed' three-dimensional cloud scene is generated over a square grid of dimension $L = 38.4$ km with equal resolution in the x and y directions of $\Delta_x (= \Delta_y) = 600$ m. A vertical grid of 45 stretched levels is used with a high resolution of 50 m in the first 2 km of the boundary layer (BL). The effect of the vertical decorrelation due to the u and w wind components is added to generate case A, assuming that a parcel of air is subject to both wind components concurrently. For each grid box (i), the initial vertical parcel position z_i is translated into a horizontal displacement according to:

$$\Delta x = \frac{(\widetilde{u}_{z_{i+1}} - \widetilde{u}_{z_i})\Delta z^2}{\int_{z_i}^{z_{i+1}} \widetilde{w}(z)\, \mathrm{d}z}, \tag{5}$$

where $\widetilde{u}(z)$ and $\widetilde{w}(z)$ are the root-mean-square values of the wind components calculated over the 40 km legs at height z. Note that Eq. (5) implies two main assumptions: that the shearing is (i) a stationary process and (ii) not acting along the y direction.

From this realization, case B is generated by removing the vertical decorrelation produced by applying Eq. (5). Finally, case C is obtained by vertically averaging the

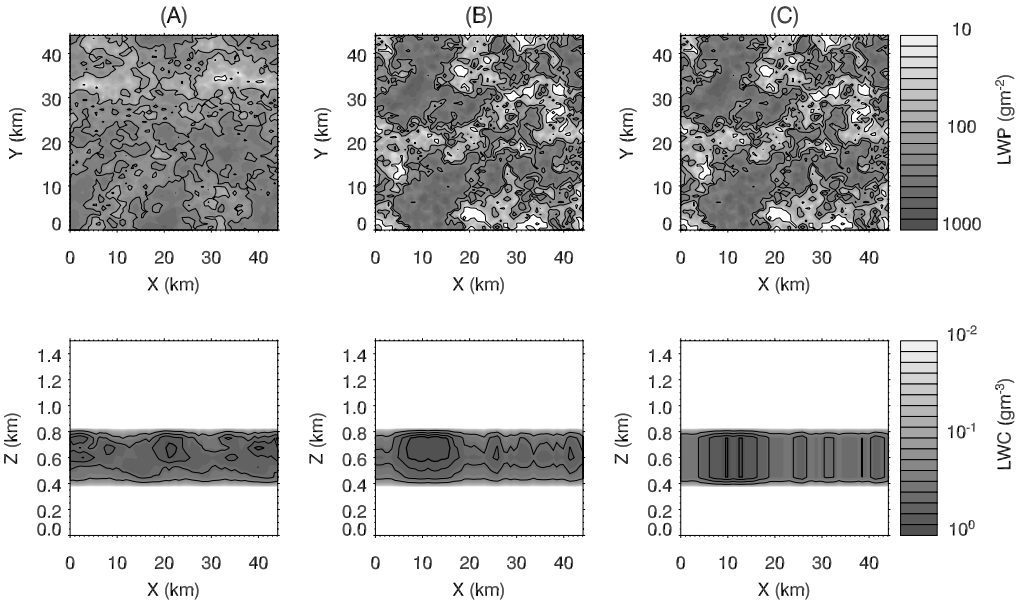

Figure 5. Upper panels: the liquid-water-path fields for the three reconstructed cloud fields A, B and C. Lower panels: x–z transects, averaged along the y direction, of the liquid-water concentration (shading levels given in the key on the right-hand side).

LWC in each column. This last realization is similar to the one obtainable with a cascade model, except that the cloud cover is less than unity. Figure 5 shows the LWP fields and vertical transects through the three cloud fields. The effects of the wind shear through case A and of the maximum overlap in case B are obvious. Note that the inclusion of the wind-shear effect in the reconstructed cloud field implies an increase in the cloud cover and a reduction in the variance of the LWP probability density function (PDF) due to smoothing of the LWP variability as shown by the higher regression coefficient obtained from the linear fit of the power spectrum in the frequency space (see Fig. 6(a)) for case A. From these three-dimensional representations, the three cloud fields are also reduced to their plane-parallel counterparts by first horizontally averaging the cloud condensate mass at each height and then rearranging the clouds according to maximum or random overlap rules usually applied in GCMs. Examining the cloud overlap at each height, the atmosphere is divided up into the number of columns required to capture the vertical cloud structure. This method is identical to the one performed by Di Giuseppe and Tompkins (2003b) and has also been implemented in a GCM by Collins (2001). In Fig. 7 the three cloud representations reduced to the 'PP mode' are shown. In cases B and C the maximum vertical correlation is obtained by arranging the vertical layers according to the maximum overlap rule and this results in minimal possible total cloud cover

$$\mathcal{A}^{\mathrm{B}} = \mathcal{A}^{\mathrm{C}} = \max(a_1, a_2, \ldots, a_n).$$

In case A, random overlap is assumed and, therefore, the total cloud cover for the scene is $\mathcal{A}^{\mathrm{A}} = 1 - \prod_i (1 - a_i)$. The total cloud cover in this case is, therefore, maximized.

It is important to notice that the three fields possess the same mean LWP and the same horizontal variability in LWC at each vertical layer, nevertheless case C has a different in-cloud optical depth (Slingo 1989). This is due to the assumption that the water-droplet effective radius, r, is not constant inside the cloud but is calculated in

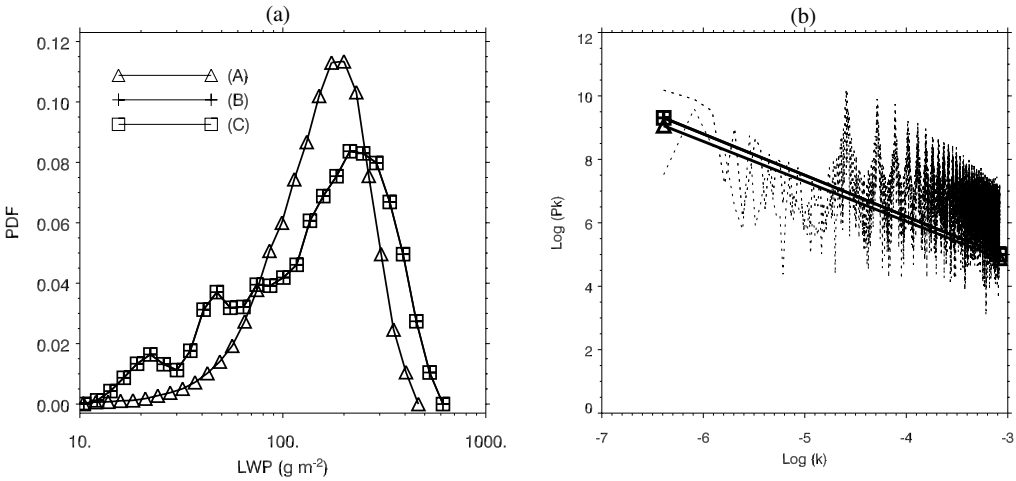

Figure 6. (a) The liquid-water path (LWP) probability density function for the three reconstructed fields A, B and C. (b) The LWP power spectra for the three cases. The solid lines represent the linear regression of the power spectra.

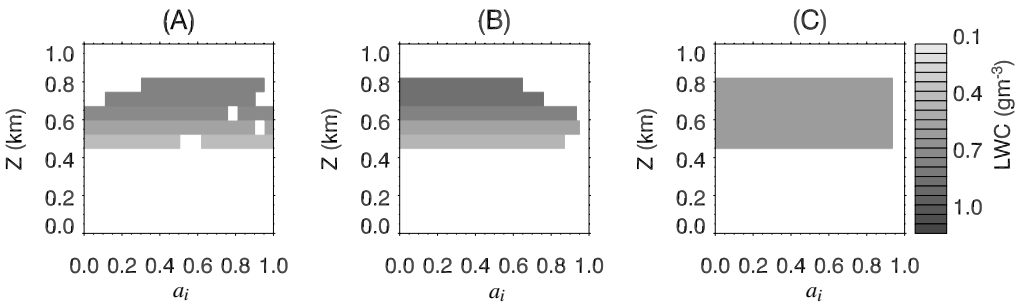

Figure 7. Liquid-water contents in each layer (see key for shading levels) of cloud-field experiments A, B and C, reduced to plane-parallel and homogeneous representations. The horizontal axis indicates the mean cloud cover (a_i) associated with the layers.

order to maintain the number of water droplets, N, constant, in agreement with that observed during the aircraft measurement (Pontikis 1993; Los and Duynkerke 2000)*:

$$r = \sqrt[3]{\frac{3\mathrm{LWC}}{4\pi\rho_{\mathrm{l}}N}}, \tag{6}$$

where ρ_{l} is the water density and LWC is the liquid-water content. With this assumption, the in-cloud optical depth can be calculated for each given vertical column as (see also Stephens 1990):

$$\tau_{\mathrm{cld}} = \underbrace{\left(\frac{9}{2}\pi\frac{N}{\rho_{\mathrm{l}}^2}\right)^{1/3}}_{\mathcal{D}} \int_{z_{\mathrm{b}}}^{z_{\mathrm{t}}} \mathrm{LWC}^{2/3}(z)\,\mathrm{d}z, \tag{7}$$

* This expression for r is exact only for mono-dispersive droplet-size distributions. For poly-dispersive droplet-size distributions it underestimates its value by about 10% (Martin *et al.* 1994).

TABLE 1. MAIN THERMODYNAMICAL AND OPTICAL PARAMETERS OF THE CLOUD SCENES REPRODUCED IN EXPERIMENTS A, B AND C FOR THE THREE-DIMENSIONAL FIELDS USED IN THE 3D AND IPA CALCULATIONS AND THE 1D FIELDS USED IN THE PP APPROXIMATION (SEE TEXT FOR AN EXPLANATION OF THE SYMBOLS)

	Experiment A		Experiment B		Experiment C	
Quantity	3D	PP	3D	PP	3D	PP
μ_{LWP} (g m^{-2})	180	176	193	193	193	193
$\sigma_{\mathrm{LWP}}/\mu_{\mathrm{LWP}}$	0.46	0.26	0.66	0.21	0.66	0.00
$\mathcal{A}$	1.00	1.00	0.93	0.93	0.93	0.93
τ_{cld}	22.95	22.45	24.15	24.15	24.15	24.14
N	130	130	130	130	130	130
z_{t} (km)	0.75	0.75	0.75	0.75	0.75	0.75
z_{b} (km)	0.45	0.45	0.45	0.45	0.45	0.45

All the quantities are averaged on in-cloud pixels only.

where z_{t} and z_{b} are the column top and bottom heights. The assumption of a variable effective radius inside the cloud leads to a nonlinear relationship between the LWC and the columnar optical depth.

If the cloud liquid-water gradient (that we can assume adiabatic), Γ_{l}, is resolved, as in cases A and B here, then Eq. (7) becomes:

$$\tau^{\mathrm{A,B}} = \mathcal{D}\tfrac{3}{5}\Gamma_{\mathrm{l}}^{2/3}(z_{\mathrm{t}} - z_{\mathrm{b}})^{5/3}, \tag{8}$$

with $\mathcal{D} = \{\frac{9}{2}\pi(N/\rho_{\mathrm{l}}^2)\}^{1/3}$, while if the cloud is vertically homogeneous, as in case C, Eq. (7) reduces to:

$$\tau^{\mathrm{C}} = \mathcal{D}\frac{\Gamma_{\mathrm{l}}^{2/3}}{2^{2/3}}(z_{\mathrm{t}} - z_{\mathrm{b}})^{5/3}. \tag{9}$$

Since, for each vertical column, the optical depth calculated from Eq. (9) is systematically 5% larger than the one evaluated using Eq. (8), this increase will also apply to the domain-averaged optical depth, provided that the two cloud scenes have the same cloud cover (P. Räisänen 1999). This difference can be even larger for more complex LWC profiles.

Clouds possessing the same horizontal variability in their integrated LWC (i.e. liquid-water path) will not, in general, have the same mean τ if they do not have, in each horizontal column, the same LWC profile for the reasons given above. On the other hand, two cloud fields that only varied in the vertical overlap applied between adjacent cloud layers (as between cases A and B here) will have still identical mean optical depths. Changing from maximum to random overlap introduces neither variations in the optical depth of the cloud scene nor changes in the cloud-fraction vertical profile. Nevertheless, as shown in section 6, it strongly affects the radiative properties of the cloud scene (Morcrette and Fouquart 1986). Therefore, the use of the optical depth alone is not sufficient, even in a one-dimensional radiative calculation, for a correct flux calculation when in presence of a vertically extended cloud system. In Table 1 the main microphysical and optical characteristics of the three cloud scenes are summarized. Values are reported for both the 3D fields used in the 3D and IPA calculations and for the 1D representations used in the PP approximation. Note how the *in-cloud* LWP variability, documented as relative standard deviation ($\sigma_{\mathrm{LWP}}/\mu_{\mathrm{LWP}}$), is maximum for the 3D field of case C and minimum (constant field) for the same scene when reduced to a 1D field. It is then predictable that this case should produce the largest 1D biases.

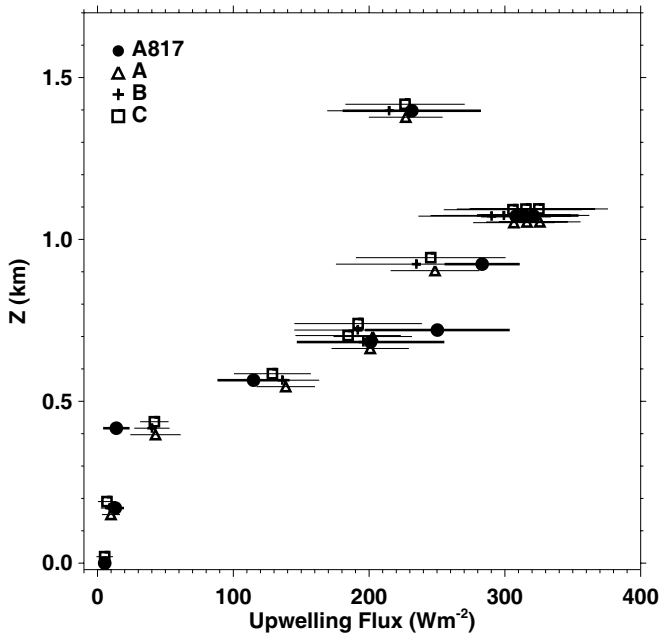

Figure 8. Mean upwelling fluxes for the measured and simulated radiation fields A, B and C (see text). The mean values have been calculated for the 13 legs of 40 km. The horizontal bars indicate the standard-deviation intervals.

5. Comparison between modelled and measured fluxes

In this section, the properties of radiative fields computed using the three reconstructed fields are compared with aircraft measurements. The mean upwelling and downwelling fluxes along the 13 legs of 40 km length into which the A817 flight has been divided are examined. The simulated fluxes are calculated for a SZA equal to 65° and then rescaled for the cosine of the measured mean SZA along the 13 transects. Figure 8 shows the mean upwelling fluxes and the standard-deviation intervals for the vertical profiles along the legs of 40 km length, and highlights the substantial variability in the observed values. For example, the three legs flown at 1.07 km can have flux differences of up to 50 W m^{-2}. For the majority of the data points, the standard-deviation intervals of the observations and the simulated fields overlap. Nevertheless, the mean values for cases A, B, and C are almost always closer to each other than to the measurements. This probably occurs because there are significant uncertainties in the modelled cloud fields (not only due to deficiencies in SITCOM but also due to incomplete cloud-field sampling by the aircraft) and in the sampling of observed radiation fields. The comparison of mean fluxes with the measurements is not necessarily a good metric for assessing the realism of cloud representations. The sensitivity of domain-average fluxes to mean microphysical properties implies that this agreement could also be obtained by tuning various model parameters, such as the mean effective water-droplet radius. A more stringent test is to compare the variability of the fluxes over the simulated cases with the real measurements, since this is dependent on the generated inhomogeneities in the reconstructed cloud fields and not on averaged optical properties.

An estimate of the agreement in the flux variability between the generated cloud fields and the measurements can be obtained by comparing the PDF of the perturbation anomaly around the mean in the upwelling and downwelling fluxes along the legs for the

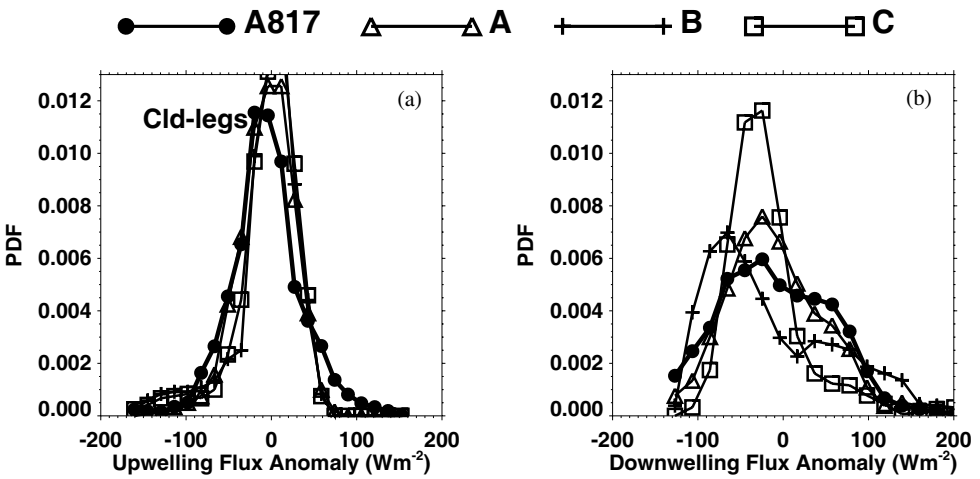

Figure 9. Comparison between the (a) upwelling and (b) downwelling flux probability density functions for the data collected during flight A817 and the simulated scenes A, B and C. Only the four legs of 40 km inside the cloud have been used.

data and the simulated cases (Fig. 9). Only the four in-cloud legs have been considered, which not only contain information of the horizontal variability, but also pertain to the vertical structure. Noting the asymmetry resulting from the wind-shear decorrelation, in case A this statistical analysis has been conducted using transects along the x, y and diagonal $x - y$ directions. Since negligibly small differences were found when using different directions, here only results obtained employing the transect extracted along the x-axis are reported. The presence of the wind shear creates a smoother radiative field in case A when compared with case B. The flux anomaly PDF is, therefore, narrower in this case. Analogously, the neglect of the vertical variability (case C) produces a narrower PDF compared with case B in which the vertical cloud structure is included. This could not have been predicted looking at the identical values of $\sigma_{\mathrm{LWP}}/\mu_{\mathrm{LWP}}$ in cases B and C reported in Table 1. Therefore, it can be erroneous to use *only* vertically integrated quantities to characterize the horizontal variability of cloud fields. A Chi-squared test at 95% confidence, conducted to verify the coincidence between each of the three simulated PDFs with the observed one, is rejected only for case C.

The previous comparison of flux-anomaly PDFs is not a conclusive proof of consistency between the observations and the synthetic field, since several processes can be characterized by the same kind of variability even if they do not represent the same physical phenomenon. For further evidence, therefore, Fig. 10 shows the spectral correlation (i.e. the correlation coefficient between the simulated and observed series as a function of the scale of cloud variability—see Press *et al.* (1992) for details) for the net flux (downward-minus-upward flux) in the thirteen legs of 40 km length between the observations and the simulated transects along the x directions. Flux series derived from simulated fields have been interpolated in order to obtain the same sample dimensions as the measured data prior to cross-spectral analysis. Values obtained for length scales smaller than the Nyquist frequency of the reconstructed fields ($2 \times \Delta_x = 1.2$ km) are not reported in Fig. 10. The 95% confidence level is also shown, outlining the significant level of correlation between cases A and B and the observations, especially for spatial scales between 10 and 30 km. Most of the case C values lie underneath the 95%

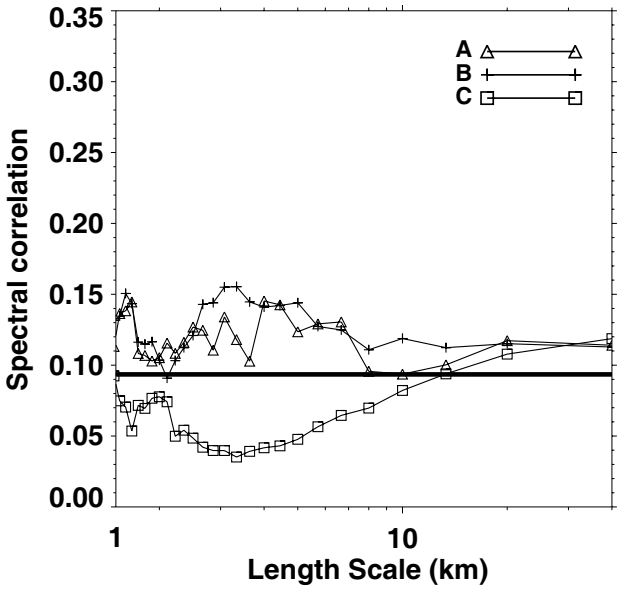

Figure 10. Spectral correlation of the net flux (downward minus upward flux) in the thirteen 40 km legs between the observations and the simulated transects A, B and C along the x, y and (diagonal) $x - y$ directions, shown as a function of the scale of cloud variability. The horizontal solid line represents the 95% confidence levels. Values above this line are statistically in agreement with the observations while values below it are not. See text for details.

confidence level. In this case, the exclusion of the vertical cloud structure introduces a substantial disagreement with the observations.

6. Analysis of area-mean cloud radiative properties

While cases A and B perform well in reproducing observed radiative-flux variations for the Sc cloud, case C showed statistically significant differences. In this section it is investigated how those differences affect area-mean cloud-radiative properties and modify the assessment of 1D biases.

In addition to the full 3D radiative-transfer calculation, two simplified calculations based on the IPA and PP approximations are performed. To avoid uncertainty, the same radiative algorithm is used for each mode of calculation, with simplifications applied to mimic the IPA and PP methods. The IPA calculation is obtained by constraining each single column of the 3D atmospheric field to have periodic boundary conditions. In this way, the horizontal transport of radiation is eliminated while conserving the horizontal optical inhomogeneity. The PP calculation is obtained by applying the IPA calculation to the homogeneous cloud fields presented in Fig. 7.

The differences in the area-mean cloud radiative properties between cases A and B quantify the error produced by inexact vertical overlap assumptions. If this comparison is performed using the A/PP and B/PP calculations, only the bias due to vertical overlap between adjacent layers can be assessed, while if the difference in the two A/IPA and B/IPA calculations is used this also includes the effect due to different overlap between in-cloud inhomogeneities. Finally, if A/3D and B/3D calculations are compared, information is obtained about possible changes in the horizontal-flux fields induced by the different overlap between horizontal inhomogeneities. In overcast Sc

clouds, the horizontal transport of radiation is negligible (Cahalan *et al.* 1994b) and, in fact, the A/IPA and B/IPA calculations are remarkably close to the corresponding 3D ones. This last effect can, therefore, be ignored and so is not discussed in the following sections.

The contrast in the area-mean cloud radiative properties calculated for cases B and C quantifies the radiative biases due to unresolvable LWC vertical profiles. Differences in B/PP and C/PP calculations quantify the radiative bias produced by a degradation in the vertical resolution of the model. This case would be equivalent to comparing two GCMs with different vertical resolutions. Differences between B/IPA and C/IPA will also include the effect due to horizontal inhomogeneities. Therefore, this case would be equivalent to comparing two GCMs with different vertical resolutions in which the subgrid-scale variability of clouds is also taken into account.

To summarize, if the contrast between 3D and 1D calculations using the same cloud representations quantifies the radiative biases due to the neglect of horizontal inhomogeneities and horizontal transport of radiation, the differences between calculations performed across cloud representations quantify the bias introduced by vertical overlap rules and by the neglect of vertical cloud structures. Figure 11 shows the top-of-the-atmosphere reflection, transmission to the ground and atmospheric absorption for the three reconstructed cloud scenes calculated using the 3D, IPA and PP methods as a function of the SZA. It is notable how variation due to the cloud representation (for example, A/3D, B/3D, and C/3D) is comparable to that due to the use of a 1D approximation for a particular scene (for example, A/3D when compared with A/PP). The assumptions on vertical cloud structures are, therefore, not less important than the ones due to horizontal inhomogeneities. In the next two sections these two factors are analysed separately.

(*a*) *Biases due to unresolved vertical variability*

Figure 12 shows the effect of vertical variability on area-mean cloud-radiative properties by comparing the relative atmospheric reflection across the three cases A, B and C, using all three methods 3D, IPA and PP of calculation. The differences between the A/PP and B/PP reflections are mainly due to the different *total* cloud cover of the two scenes. This is demonstrated noting that the difference of 6% in reflection is identical to the total cloud fraction increase (Table 1) between the two cases, and is obviously not SZA dependent. The inclusion of horizontal variability (A/IPA and B/IPA) further increases the bias by an additional 3% for very high SZA. This is due to the fact that only case A/IPA accounts for vertical decorrelation of cloud-water distributions and has, therefore, a smaller horizontal variance of LWP. Adding the horizontal transport of radiation (A/3D compared with B/3D) does not introduce any significant effects at high sun angles, and only decreases the biases for very oblique sun positions, in agreement with Cahalan *et al.* (1994b) and Di Giuseppe and Tompkins (2003b). The differences in reflection between experiments B/PP and C/PP are smaller than the code accuracy. Moreover, no significant differences are noticeable if the horizontal in-cloud variability is taken into account. In fact the differences between the two scenes are null, even when using the IPA or the 3D calculations.

Nevertheless, the very small effect produced by the 5% increase in optical depth between cases B and C (discussed in section 4) can be due to the high optical opacity of the cloud scene investigated here. To quantify the range of possible biases expected in cloud systems with smaller optical depths, the rate of change in the reflection due to variations in τ_{cld} is estimated by using the tangent-linear formulation for the reflection following the δ-Eddington approximation for conservative scattering. The change of

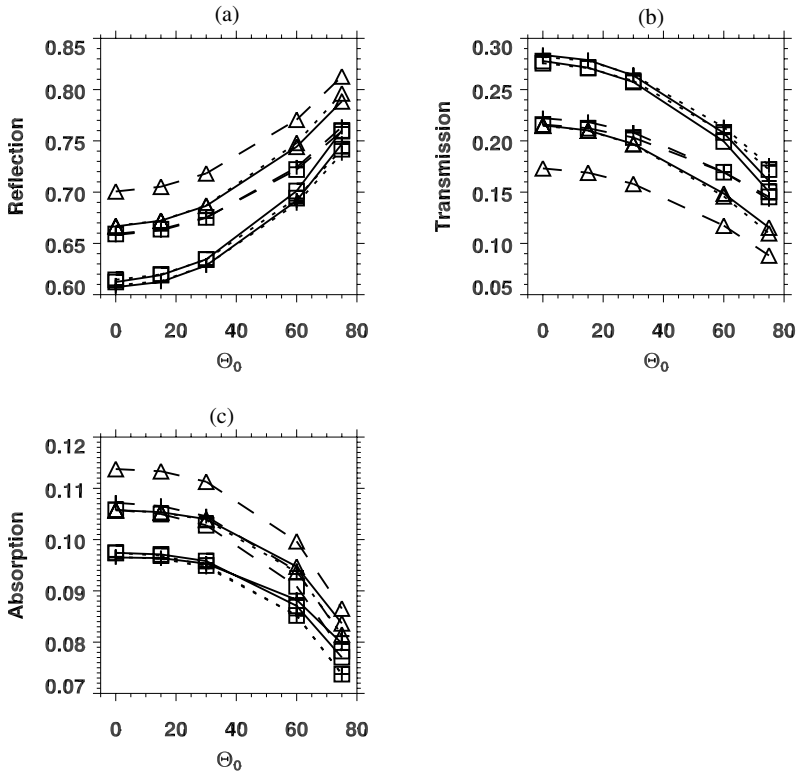

Figure 11. Top-of-the-atmosphere (a) reflection, (b) transmission to the ground and (c) atmospheric absorption for the three reconstructed cloud scenes A (△), B (+) and C (□) calculated using the 3D (solid line), IPA (dotted line) and PP (dashed line) methods (see text) as a function of the solar zenith angle Θ_0 (see key for an explanation of the symbols and line types).

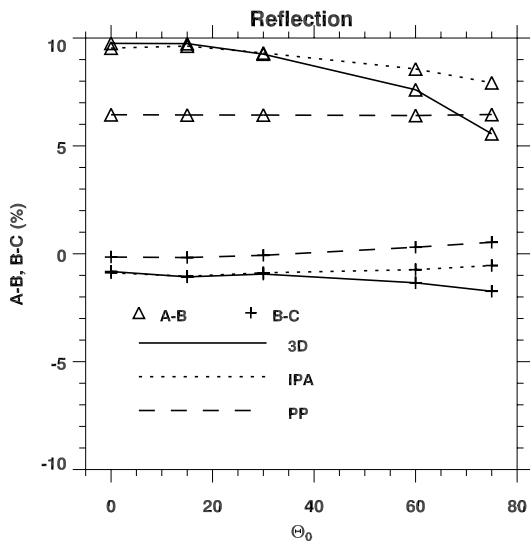

Figure 12. Relative differences (%) in the reflection between experiments A and B (△) and experiments B and C (+) as a function of the solar zenith angle, Θ_0. The differences are plotted for the 3D (solid lines), IPA (dotted lines) and PP (dashed lines) radiative calculations.

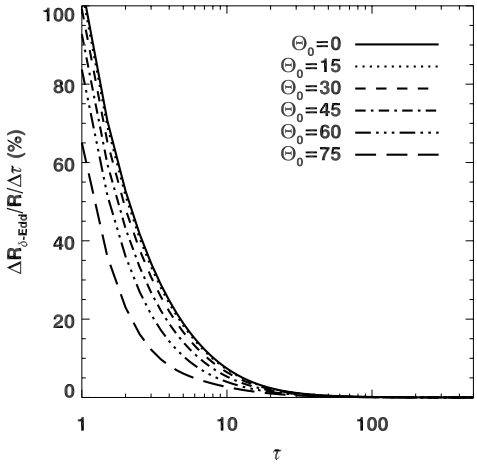

Figure 13. Relative variation in the reflection ($\Delta R_{(\delta\text{-Eddington})}/\Delta\tau$) as a function of unitary change in the cloud optical depth (τ) following the δ-Eddington approximation for conservative scattering for a range of solar zenith angles, Θ_0. The asymmetry parameter $g = 0.87$.

$\Delta R_{(\delta\text{-Eddington})}/\Delta\tau$ as function of τ is shown in Fig. 13 for a range of solar zenith angles, Θ_0, and asymmetry parameter $g = 0.87$. The estimated increase in reflection due to 5% change in τ_{cld} is around 0.5% for an optical depth $\tau \approx 20$ (see Table 1). This value is comparable with the code accuracy, and is in agreement with the results in Fig. 11. Notably, an increase of 5% in the optical depth of a cloud field with $\tau = 1$ would result in a much more substantial increase in reflection of 5% at an SZA equal to 0°. As a consequence, a GCM with low vertical resolution is likely to overestimate the reflection of shallow-cloud systems, even if a representation of the subgrid-scale horizontal variability is present.

(*b*) *Bias due to unresolved horizontal variability*

The effect of horizontal variability on area-mean cloud radiative properties is analysed by comparing 1D biases inside each cloud representation. Figure 14 shows the PP (defined as (IPA–PP)/PP) and IPA (defined as (3D–IPA)/IPA) relative biases (Cahalan *et al.* 1994b) calculated for the three cases A, B and C and for the total atmospheric reflection, transmission and absorption as a function of the SZAs. In *overcast* stratocumulus clouds horizontal transport of radiation plays a minor role, the IPA bias for all three experiments is zero for high sun angles and is in within a few percent in the reflection as the SZA increases. Interestingly, the A/IPA bias has the opposite sign to that of B/IPA and C/IPA, both in the reflection and transmission.

The C/PP bias is maximized with a 7.4% decrease in the reflection and a 27.4% increase in the transmission when the sun is overhead. Resolving cloud vertical structures (B/PP bias) has the effect of reducing the bias. Di Giuseppe and Tompkins (2003b) explained this effect by noting the capability for a GCM's radiation scheme to appreciate the presence of horizontal variability when the cloud vertical structure is resolved due to the two-column approximation. This capability is inhibited in the vertically-homogeneous representation of the cloud field and is maximized in the representation characterized by wind-shear decorrelation, since this effectively increases the number of GCM subcolumns. When vertical decorrelation is introduced (A/PP), the PP bias is

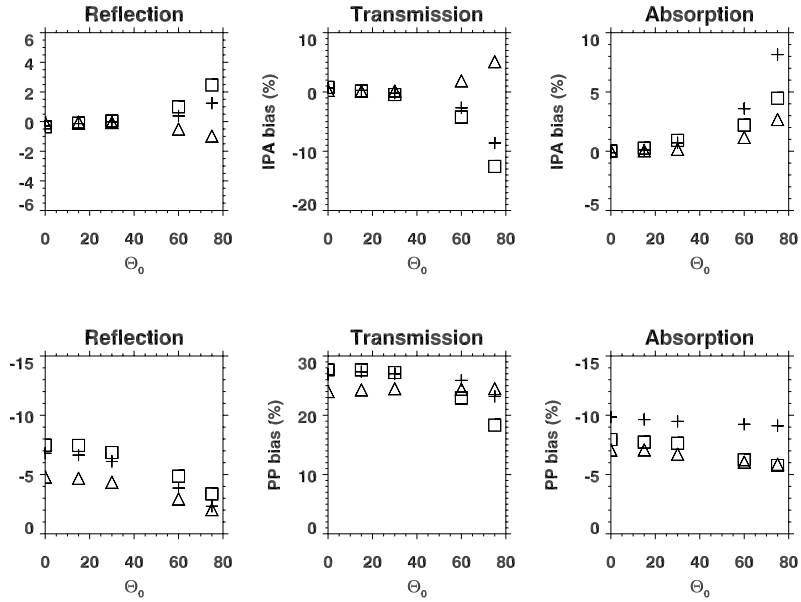

Figure 14. PP and IPA relative biases calculated for the three cases A (△), B (+) and C (□) and for the total atmospheric reflection, transmission and absorption as a function of the solar zenith angle, Θ_0.

even smaller. This is not surprising considering that the variability of optical depth in case A is the smallest.

7. Conclusions

Simple statistical models are often used to generate cloud fields as input for successive 3D radiative studies. Underlying assumptions and approximations in the representation of the cloud-field variability can lead to distortions of 1D bias assessments. In this work, employing a specific case study of nearly overcast stratocumulus cloud, the sensitivity of one-dimensional radiative biases to assumptions on the vertical cloud structure is investigated.

Three different 3D cloud fields were reconstructed using aircraft thermodynamical observations collected by the Met Office C-130 Hercules aircraft over sea near Cornwall, and a simple statistical model based on a Fourier technique described previously by Di Giuseppe and Tompkins (2003b). The control case (case A) includes both the adiabatic liquid-water profile and the vertical decorrelation produced by horizontal wind shear, the second experiment (case B) assumes maximum overlap between adjacent layers. Finally, the third cloud field (case C) is obtained by vertically averaging the in-cloud liquid water in each column to obtain a representation similar to that produced by a cascade model (Marshak *et al.* 1997b). Thus, all representations present identical mean LWPs, while the total cloud cover and the shape of the LWP distribution (variance) differ in case A with respect to the other two cases due to the vertical decorrelation.

The performance of these reconstruction processes was verified by comparing Monte Carlo simulated solar fluxes against recorded flux measurements. Cases A and B, in which both horizontal and vertical variability were included, agreed with observed (horizontal) flux variations within statistical uncertainty, while case C, which neglected vertical variability, was not able to reproduce the observed fluxes.

The relevant feature in the generation of the three cloud fields is that information about the vertical structures of the observed Sc system is progressively rejected. Therefore, comparing the three scenes' radiation fields provides an insight as to how partial cloud representation can affect the radiative calculations. In particular, the difference in area-mean cloud radiative properties between cases A and B quantifies the biases expected due to inexact vertical overlap assumptions. The contrast between the radiative fields produced in cases B and C assesses the errors due to unresolvable LWC profiles.

Analysis of area-mean cloud radiative properties for scenes A, B and C was performed using a full 3D algorithm, an independent pixel approximation (IPA) and a plane parallel (PP) approach in order to estimate additionally which metric biases due to unresolved vertical cloud structures are sensitive to horizontal variability.

The vertical homogenization of an adiabatic monotonically increasing liquid-water profile produces a systematic increase of 5% in the cloudy-column optical depth if the effective radius of the water-droplet distribution is determined by imposing, at each vertical layer, a constant number of water droplets. For the cloud scene investigated here, this was found to be of minor importance because of the high opacity of this cloud scene. However, it was also shown that, in thin clouds with optical depths around unity, this increase is likely to create an overestimation by as much as 5% in the reflection calculated with GCMs of low vertical resolution.

An even larger impact in the reflection transmission and absorption of the cloud scene was due to the variation in cloud cover produced by different overlap rules owing to the linear relation between the cloud fraction and the scene reflection and transmission. The magnitude of these biases was only weakly modified when the horizontal variability was included. Therefore, a GCM with low vertical resolution is likely to overestimate reflection of shallow-cloud systems even if subgrid-scale horizontal variability is included.

Comparing the magnitude of the PP biases between the three scenes, it was found that the bias due to the neglect of horizontal variability is enhanced if vertical inhomogeneities are not represented. This results confirms the claim of Di Giuseppe and Tompkins (2003b) that a GCM's radiation scheme, in theory, can improve on previous estimates of PP biases, provided adequate vertical resolution is used.

In summary, an insufficient knowledge of the vertical cloud structures can lead to erroneous estimation of the radiative properties of the cloud scene, even if parametrizations of the horizontal subgrid-scale variability are included. It is, therefore, suggested that more emphasis is devoted to the simultaneous treatment of the horizontal and vertical inhomogeneities, as in the initial considerations of Jeffery and Austin (2003).

ACKNOWLEDGEMENTS

The observational data used in this paper was provided by the Met Office Met Research Flight and the author is grateful to Andreas Keil and Jonathan Taylor for arranging this provision. Ronald Scheirer and Andreas Macke are thanked for making their code GRIMALDI publicly available and giving advice on its use. Anthony Slingo and Alexander Marshak are thanked for reading an early version of the manuscript and providing many useful suggestions. Adrian Tompkins is thanked for the stimulating discussions on subgrid-scale variability of clouds. Two anonymous reviewers carefully read the manuscript and provided many useful suggestions that highly improved the legibility and scientific clarity of the paper. The author was supported by the Natural Environment Research Council (contract number GT/4/00/217).

REFERENCES

Albrecht, B. A., Bretherton, C. S., Jonson, D. W., Schubert, W. H. and Frisch, A. S. 1995 The Atlantic stratocumulus transition experiment—ASTEX. *Bull. Amer. Meteorol. Soc.*, **76,** 889–904

Barker, H. W. and Davies, J. A. 1992 Solar radiative fluxes for stochastic, scale invariant broken cloud fields. *J. Atmos. Sci.*, **49,** 1115–1126

Barker, H. W., Morcrette, J. J. and Alexander, G. D. 1998 Broadband solar fluxes and heating rates for atmospheres with 3D broken clouds. *Q. J. R. Meteorol. Soc.*, **124,** 1245–1271

Barker, H. W., Stephens, G. L. and Fu, Q. 1999 The sensitivity of domain-averaged solar fluxes to assumptions about cloud geometry. *Q. J. R. Meteorol. Soc.*, **125,** 2127–2152

Cahalan, R. F. and Joseph, J. H. 1989 Fractal statistics of cloud fields. *Mon. Weather Rev.*, **117,** 261–272

Cahalan, R. F. and Snider, J. B. 1989 Marine stratocumulus structure. *Remote Sensing Environ.*, **28,** 95–107

Cahalan, R. F., Ridgway, W. and Wiscombe, W. J. 1994a Independent pixel and Monte Carlo estimates of stratocumulus albedo. *J. Atmos. Sci.*, **51,** 3776–3790

Cahalan, R. F., Ridgway, W., Wiscombe, W. J., Bell, T. L. and Snider, J. B. 1994b The albedo of fractal stratocumulus clouds. *J. Atmos. Sci.*, **51,** 2434–2455

Chambers, L. H., Wielicki, B. A. and Evans, K. F. 1997 Independent pixel and two-dimensional estimates of Landsat-derived cloud field albedo. *J. Atmos. Sci.*, **54,** 1525–1532

Collins, W. D. 2001 Parameterization of generalized cloud overlap for radiative calculations in general circulation models. *J. Atmos. Sci.*, **58,** 3224–3242

Davis, A., Marshak, A., Cahalan, R. and Wiscombe, W. 1997 The Landsat scale break in stratocumulus as a three-dimensional radiative transfer effect: Implications for cloud remote sensing. *J. Atmos. Sci.*, **54,** 241–260

Di Giuseppe, F. and Tompkins, A. M. 2003a Three dimensional radiative transfer in tropical deep convective clouds. *J. Geophys. Res.*, **108,** 10.1029/2003JD003392

2003b Effect of spatial organisation on solar radiative transfer in three-dimensional idealized stratocumulus cloud fields. *J. Atmos. Sci.*, **60,** 1774–1794

Feind, R. E., Detwiler, A. G. and Smith, P. L. 2000 Cloud liquid water measurements on the armored T-28: Intercomparison between Johnson–Williams cloud water meter and CSIRO (King) liquid water probe. *J. Atmos. Ocean. Technol.*, **17,** 1630–1638

Fu, Q. and Liou, K. N. 1992 On the correlated k-distribution method for radiative-transfer in nonhomogeneous atmospheres. *J. Atmos. Sci.*, **49,** 2139–2156

Fu, Q., Cribb, M. C., Barker, H. W., Krueger, S. K. and Grossman, A. 2000 Cloud geometry effects on atmospheric solar absorption. *J. Atmos. Sci.*, **57,** 1156–1168

Hogan, R. J. and Illingworth, A. J. 2000 Deriving cloud overlap statistics from radar. *Q. J. R. Meteorol. Soc.*, **126,** 2903–2909

Jeffery, C. A. and Austin, P. H. 2003 Unified treatment of thermodynamic and optical variability in a simple model of unresolved low clouds. *J. Atmos. Sci.*, **60,** 1621–1631

Lin, B. and Rossow, W. B. 1994 Observations of cloud liquid water path over oceans—optical and microwave remote sensing methods. *J. Geophys. Res.*, **99,** 20907–20927

Los, A. and Duynkerke, P. G. 2000 Microphysical and radiative properties of inhomogeneous stratocumulus: Observations and model simulations. *Q. J. R. Meteorol. Soc.*, **126,** 3287–3307

2001 Parametrization of solar radiation in inhomogeneous stratocumulus: Albedo bias. *Q. J. R. Meteorol. Soc.*, **127,** 1593–1614

Macke, A., Mueller, J., Nagel, K. and Stuhlmann, R. 1997 'A cellular automaton model for cloud formation: Radiative properties'. Pp. 234–237 in *Current problems in atmospheric radiation*, Eds. W. Smith and K. Stamnes, A. Deepak Publishing, Hampton, Virginia, USA

Marshak, A., Davis, A., Wiscombe, W. and Cahalan, R. F. 1997a Inhomogeneity effects on cloud shortwave absorption measurements: Two-aircraft simulations. *J. Geophy. Res. Atmos.*, **102,** 16619–16637

	1997b	Scale invariance in liquid water distributions in marine stratocumulus: Multifractal properties and intermittency issues. *J. Atmos. Sci.*, **54,** 1423–1444
Martin, G. M., Johnson, D. W. and Spice, A.	1994	The measurement and parameterization of effective radius of droplets in warm stratocumulus clouds. *J. Atmos. Sci.*, **51,** 1823–1842
McClatchey, R. A., Fenn, R. W., Selby, J. E. A., Volz, F. E. and Garing, J. S.	1972	'Optical properties of the atmosphere'. Tech. Rep. AFCRL-72-0497, Hanscom Air Force Base, Bedford, Mass, USA
Morcrette, J. J.	1991	Radiation and cloud radiative properties in the European Centre for Medium-Range Forecasts forecasting system. *J. Geophys. Res.*, **96,** 9121–9132
Morcrette, J. J. and Fouquart, Y.	1986	The overlapping of cloud layers in shortwave radiation parameterizations. *J. Atmos. Sci.*, **43,** 321–328
Nucciarone, J. J. and Young, G. S.	1991	Aircraft measurements of turbulence spectra in the marine stratocumulus-topped boundary layer. *J. Atmos. Sci.*, **48,** 2382–2392
P. Räisänen,	1999	Effect of vertical resolution on cloudy-sky radiation calculations: Tests with two schemes. *J. Geophys. Res.*, **104,** 27407–27419
Pincus, R., McFarlane, S. A. and Klein, S. A.	1999	Albedo bias and the horizontal variability of clouds in subtropical marine boundary layers: Observations from ships and satellites. *J. Geophys. Res.*, **104,** 6183–6191
Pontikis, C.	1993	Parameterisation of the cloud optical thickness: Influence of clear air entrainment. *Geophys. Res. Lett.*, **20,** 2655–2658
Press, W. H., Teukolsky, S. A., Vetterling, W. T. and Flannery, B. P.	1992	*Numerical recipes in Fortran: The art of scientific computing, Second edition*. Cambridge University Press
Price, J. D. and Wood, R.	2002	Comparison of probability density functions for total specific humidity and saturation deficit humidity, and consequences for cloud parametrization. *Q. J. R. Meteorol. Soc.*, **128,** 2059–2072
Scheirer, R. and Macke, A.	2001	On the accuracy of the independent column approximation in calculating the downward fluxes in the UVA, UVB and PAR spectral ranges. *J. Geophys. Res.*, **106,** 14 301–14 312
Slingo, A.	1989	A GCM parameterisation for the shortwave radiative properties of water clouds. *J. Atmos. Sci.*, **46,** 1419–1427
Stephens, G. L.	1990	On the relationship between water vapour over the oceans and sea surface temperature. *J. Climate*, **3,** 634–645
Titov, G.	1998	Radiative horizontal transport and absorption in stratocumulus clouds. *J. Atmos. Sci.*, **55,** 2549–2560
Tompkins, A. M.	2003	Impact of temperature and humidity variability on cloud cover assessed using aircraft data. *Q. J. R. Meteorol. Soc.*, **129,** 2151–2170
Wood, R. and Field, P. R.	2000	Relationships between total water, condensed water, and cloud fraction in stratiform clouds examined using aircraft data. *J. Atmos. Sci.*, **57,** 1888–1905
Wood, R. and Taylor, J. P.	2001	Liquid water path variability in unbroken marine stratocumulus cloud. *Q. J. R. Meteorol. Soc.*, **127,** 2635–2662